X-ray structure analyses

$[(\text{anthracene})_3^{4-}(K_2^+THF_3)_2^{+2}]_1$ (Fig. 2). Space group $P\bar{1}$, $a = 9.388(2)$, $b = 13.265(2)$, $c = 14.192(2)$ Å, $\alpha = 62.876(8)$, $\beta = 85.20(1)$, $\gamma = 70.47(1)°$, $V = 1477.5(5)$ Å^3, $Z = 1$, $\rho = 1.263$ g cm^{-3}, $\mu = 0.35$ mm^{-1}, $F(000) = 598$, crystal size $= 0.4 \times 0.35 \times 0.35$ mm; crystals were removed from the trap wall after 4 days under argon, immediately immersed in perfluor-polyether oil and mounted under a flow of nitrogen cooled to 150 K on a Siemens P4 diffractometer (Mo Kα, graphite monochromator). A total of 6,211 reflections ($2.31 < \Theta < 26.27°$) were collected, of which 4,911 unique reflections ($R_{int} = 0.0308$) were used. The structure was solved using the program SHELXS-93 and refined (343 parameters) using the program SHELXS-93 to $R = 0.0434$ for 3,941 reflections with $I > 2\sigma(I)$ (both programs from G. M. Sheldrick, Univ. Göttingen, 1993).

$[(\text{anthracene})_2^{2-}(K_2^+THF_3)^{+2}]_1$ (Fig. 1c). Space group $C2/c$, $a = 14.186(3)$, $b = 10.633(2)$, $c = 23.382(4)$ Å, $\beta = 103.78(1)°$, $V = 3425.4(11)$ Å^3, $Z = 4$, $\rho = 1.262$ g cm^{-3}, $\mu = 0.314$ mm^{-1}, $F(000) = 1,384$, crystal size $= 0.25 \times 0.62 \times 0.84$ mm; crystals were removed from the trap wall after 11 days under argon, immediately immersed in perfluor-polyether oil and mounted under a flow of nitrogen cooled to 150 K on a Siemens P4 diffractometer (Mo Kα, graphite monochromator). A total of 3,783 reflections ($2.42 < \Theta < 25°$) were collected, of which 2,995 unique reflections ($R_{int} = 0.0337$) were used. The structure was solved using the program SHELXS-93 and refined (203 parameters) using the program SHELXS-93 to $R = 0.0507$ for 1,801 reflections with $I > 2\sigma(I)$ (both programs from G. M. Sheldrick, Univ. Göttingen, 1993). The β-carbon centres of the THF ligand in the middle position are disordered over two positions with site occupation factors of 0.49 and 0.51.

Unrestricted density functional theory calculations

For both the rather large aggregates $[(\text{anthracene})_3^{4-}(K_2^+THF_3)_2^{+2}]$ and $[(\text{anthracene})_2^{2-}(K_2^+THF_3)^{+2}]$, the singlet- and triplet-state computations have been performed at the UB3LYP/6-31G* level, using the NEC SX4 supercomputer of the Höchstleistungs-Rechenzentrum Stuttgart, Germany using the Gaussian 94 program package[9]. The singlet-state calculations were started from the broken symmetry orbital. The total energies of the triplet states are calculated to be −5384.72797 a.u. and −2976.24778 a.u. The charge and spin distributions were obtained by natural bond orbital analysis after enlarging the capacity of the corresponding program module.

EPR measurements

Pulsed and continuous-wave EPR measurements were performed with a Bruker E580 ELEXIS X-band spectrometer. Single crystals ($4 \times 0.35 \times 0.35$ mm) were sealed in 3-mm-diameter X-band quartz EPR capillaries under argon in n-hexane solution. The single crystals give rise to a narrow homogeneous EPR line, with a linewidth of 1.9 G and a g value close to 2, typical for a π-delocalized organic radical. No dipolar splitting of the signal could be observed in the temperature range 10–290 K. The Rabi oscillation behaviour of the signal[17] of these crystals have been compared with a spin-state $S = 1/2$ radical salt of perylene $((\text{perylenyl})_2(AsF_6)_{0.75}(PF_6)_{0.35}{\cdot}0.85\,CH_2Cl_2)$ and a spin-state $S = 5/2$ MnO sample (only the central $m_S = -1/2$ to $+1/2$ transition observed) under identical conditions (same Q value of microwave cavity, microwave excitation power, sample size and temperature). The theoretical predicted ratio of the oscillation frequencies are $1 : \sqrt{2} : 3$ for a $S = 1/2$, a $S = 1$ and the $m_S = -1/2$ to $+1/2$ transition of a $S = 5/2$ spin state. The observed Rabi frequencies were 7 MHz for $S = 1/2$, 9.5 MHz for the anthracene crystals, and 24 MHz for the MnO sample. Therefore these measurements clearly showed that the spin state of the observed signal corresponds to a triplet state. The temperature dependence (10–290 K) of the EPR signal as well as the absolute signal intensity exclude an assignment of the signal to a low-lying excited triplet state or to impurities or defects. Taken together, these measurements prove that the ground state of this compound is indeed a triplet spin state.

Received 20 July 1999; accepted 17 January 2000.

1. Lehn, J. M. *Supramolecular Chemistry, Concepts and Perspectives* (VCH, Weinheim, 1995).
2. Müller, A., Reuter, H. & Dillingers, S. Supramolecular inorganic chemistry: small guests in small and large hosts. *Angew. Chem. Int. Edn Engl.* **34,** 2326–2361 (1995).
3. Müller, A., Shah, S. Q. N., Bögge, H. & Schmidtmann, M. Molecular growth from a Mo_{176} to a Mo_{248} cluster. *Nature* **397,** 48–50 (1999).
4. Bock, H., Lehn, J. M., Pauls, J., Holl, S. & Krenzel, V. Sodium salts of the bipyridine dianion polymer$[(bpy)^{2-}\{Na^+(dme)\}_2]_x$ cluster $[(Na_8O)^{6+}Na_6^+(bpy)_6^{2-}(tmeda)_6]$, and monomer $[(bpy)^{2-}\{Na^+(pmdta)\}_2]$. *Angew. Chem. Int. Edn. Engl.* **38**, 952–955 (1999).
5. Bock, H. *et al.* The lipophilically wrapped polyion aggregate $\{[Ba_6Li_3O_2]^{11+}[^-OC(CH_3)_3]_{11}(OC_4H_8)_3\}$, a face-sharing (octahedron + prismane) $Ba_6Li_3O_2$ polyhedron in a hydrocarbon ellipsoid: preparation, single crystal structure analysis, and density functional calculations. *Angew. Chem. Int. Edn. Engl.* **34,** 1353–1355 (1995).
6. Bock, H., Gharagozloo-Hubmann, K., Näther, C., Nagel, N. & Havlas, Z. $[\{Na^+(thf)_2\}_4(\text{rubrene})^{4-}]$ crystallisation and structure determination of a contact ion quintuple for the first π-hydrocarbon-tetraanion. *Angew. Chem. Int. Edn Engl.* **35,** 631–633 (1996).
7. Sekiguchi, A., Matsuo, T. & Kabuto, C. Synthesis and characterisation of the tetralithium salt of an octasilyl-substituted trimethylencyclopentadien-tetraanion. *Angew. Chem. Int. Edn Engl.* **36,** 2462–2464 (1997).
8. Bock, H., Gharagozloo-Hubmann, K., Sievert, M. & Havlas, Z. Synthesis, crystal growth and structure determination of $[(6,13'\text{-Dipentacene}^{\ominus 4})(K^{\oplus}DME)_4]_\infty$: a twin-strand polymer helix. *Angew. Chem. Int. Edn Engl.* (submitted).
9. Havlas, Z. & Bock, H. Bare molecular anions of the saturated hydrocarbons: density functional charge and spin distribution based on their single crystal structures. *Collect. Czech. Chem. Commun.* **63,** 1245–1263 (1998).
10. Bock, H., John, A., Havlas, Z. & Bats, J. W. The triplet biradical tris(3,5-di(tert-butyl)4-oxopheny-lene)methane: crystal structure, spin and charge distribution. *Angew. Chem. Int. Edn Engl.* **32,** 416–418 (1993).
11. Bock, H., Näther, C., Ruppert, K. & Havlas, Z. Tetraphenylbutadiene disodium dimethoxyethene: solvent-shared and solvent-separated ion triples within a single crystal. *J. Am. Chem. Soc.* **114,** 6907–6908 (1992).
12. Bock, H., Näther, C., Ruppert, K. & Havlas, Z. Competing $Na^{\oplus}$ solvation: ether-shared and ether-separated triple ions of perylene dianion. *J. Am. Chem. Soc.* **117,** 3869–3870 (1995).
13. Bock, H. *et al.* Distorted molecules: perturbation design, preparation and structures. *Angew. Chem. Int. Edn Engl.* **31,** 550–581 (1992).
14. Bock, H., Näther, C., Havlas, Z., John, A. & Arad, C. Ether-solvated sodium ions in salts containing π-hydrocarbon anions: crystallisation, structures and semiempirical solvation energies. *Angew. Chem. Int. Edn Engl.* **33,** 875–878 (1994).
15. Bock, H., Arad, C., Näther, C. & Havlas, Z. The structure of solvent-separated naphthalene and anthracene radical anions. *J. Chem. Soc. Chem. Commune.* 2393–2394 (1995).
16. Rhine, W. E., Davis, J. & Stucky, G. Anthracene dianion dilithium bis(TMEDA). *J. Am. Chem. Soc.* **97,** 2079–2085 (1975).
17. Stoll, S., Jeschke, G., Willer, M. & Schweiger, A. Nutation-frequency correlated EPR spectroscopy: the PEANUT experiment. *J. Magn. Reson.* **130,** 86–96 (1998).

Acknowledgements

We thank T. Hauck for the first crystal growth, C. Näther and S. Holl for structure determination, V. Krenzel for graphics, and J. T. Töring & H. Käß for EPR measurements. This work was supported by the Deutsche Forschungsgemeinschaft, the Fonds der Chemischen Industrie and the State of Hesse.

Correspondence and requests for materials should be addressed to H.B. (e-mail: bock@www.anorg.chemie.uni-frankfurt.de). Further details of crystal growth and structure determination may be obtained from the Cambridge Crystallographic Data Centre (12 Union Road, Cambridge CB2 1EZ, UK) on quoting supplementary publication no. CCDC-137565 for the compound shown in Fig. 2, and no. CCDC-137566 for the compound shown in Fig. 1c.

Seismic hazard in the Marmara Sea region following the 17 August 1999 Izmit earthquake

Aurélia Hubert-Ferrari*, Aykut Barka†, Eric Jacques‡, Süleyman S. Nalbant§, Bertrand Meyer‖, Rolando Armijo‖, Paul Tapponnier‖ & Geoffrey C. P. King‖

* *Department of Geosciences, Princeton University, Princeton, New Jersey 08544, USA*
† *ITU, Maden Fakultesi, Jeoloji Bolumu, Ayazaga, Istanbul, Turkey*
‡ *Observatoire des Sciences de la Terre de Strasbourg (UMS 830 of CNRS), Strasbourg, France*
§ *Geophysics Department, Engineering Faculty, Istanbul University, Istanbul, Turkey*
‖ *Laboratoire de Tectonique et Mécanique de la Lithosphère (UMR 7578 of CNRS), Institut de Physique du Globe, Paris*

On 17 August 1999, a destructive magnitude 7.4 earthquake occurred 100 km east of Istanbul, near the city of Izmit, on the North Anatolian fault. This 1,600-km-long plate boundary[1,2] slips at an average rate of 2–3 cm yr^{-1} (refs 3–5), and historically has been the site of many devastating earthquakes[6,7]. This century alone it has ruptured over 900 km of its length[6]. Models of earthquake-induced stress change[8] combined with active fault maps[9] had been used to forecast that the epicentral area of the 1999 Izmit event was indeed a likely location for the occurrence of a large earthquake[9,10]. Here we show that the 1999 event itself significantly modifies the stress distribution resulting from previous fault interactions[9,10]. Our new stress models take into account all events in the region with magnitudes greater than 6 having occurred since 1700 (ref. 7) as well as secular interseismic stress change, constrained by GPS data[11]. These models provide a consistent picture of the long term spatio–temporal behaviour of the North Anatolian fault and indicate that two events of magni-

tude equal to, or greater than, the Izmit earthquake are likely to occur within the next decades beneath the Marmara Sea, south of Istanbul.

Seventy kilometres east of Izmit, the North Anatolian fault (NAF) splits into two main segmented strands[12]. The northern most active strand (NNAF) passes beneath the Sea of Marmara, while the southern strand (SNAF) remains on land south of the Sea[5,9]. Since 1900 and before the Izmit event, five earthquakes of magnitude $6 \leq M < 7$ and three $M > 7$ earthquakes have ruptured fault segments of one or other of the strands[9] (Fig. 1a). Each of the $M > 7$ earthquakes, whose fault parameters are constrained by instrumental data and surface rupture mapping, broke several segments[9]. They provide a guide to the assessment of slip during earlier $M > 7$ historical events.

The Coulomb stress[8,13] field resulting from all earthquakes this century in the Marmara Sea region before the Izmit event is shown in Fig. 1a (ref. 9). The 1963 and 1967 earthquakes enhanced stress by 0.5–2 bar in the Izmit epicentral region[9,10]. Over the last few years microseismicity had clustered around the August 1999 epicentre (Izinet network, Kandilli Observatory). The 1999 rupture nucleated in the area of increased stress, and extended along at least 110 km on four main segments (Fig. 1a) with dextral displacement of up to 5 m (ref. 1). As a result, the Coulomb stress resolved onto faults west of the rupture rose by 1–5 bar over a distance of 25 km, increasing the probability of an earthquake closer to Istanbul (Fig. 1b). At the eastern tip of the rupture, stress was increased by 10–0.6 bar along the Ducze fault, which then ruptured on 12 November 1999 with up to 5 m of dextral slip and locally up to 4 m of vertical offset. The events have also reduced stress by 3–15 bar along 120 km of the SNAF making an event there in the near future less likely (Fig. 1b). The largest aftershocks (Kandilli Observatory, preliminary locations) fall near the rupture or at rupture segment extremities where the Coulomb stress was enhanced (Fig. 1c). When earlier seismicity is included, most of the aftershocks at the western end of the rupture are confined to the area of Coulomb stress increase (Fig. 1c). This indicates that the small stress shadow of the $M = 6.4$ 1963 earthquake still persists after more than 36 years (refs 9, 13, 14).

The seismic behaviour of the NAF can be seen better in Coulomb models that include all $M > 6$ events since 1700 (see below). For the period 1700–1900, the information about damage is available. When combined with detailed mapping of Holocene faulting[9] and scaling relations[9,15] the modelling parameters (fault locations, dimensions, strike, dip, amplitude and rake of the slip vector) can be evaluated (see Methods). We also included tectonic loading in the modelling, a significant effect as the NAF has a high slip rate. We assume that associated localized shear occurs aseismically below a prescribed locking depth[16], which we model using vertical dislocations positioned beneath the mean location of the surface faults and with slip vectors that fit local GPS data around the Marmara Sea (See Methods and Fig. 2). Both this tectonic loading and the

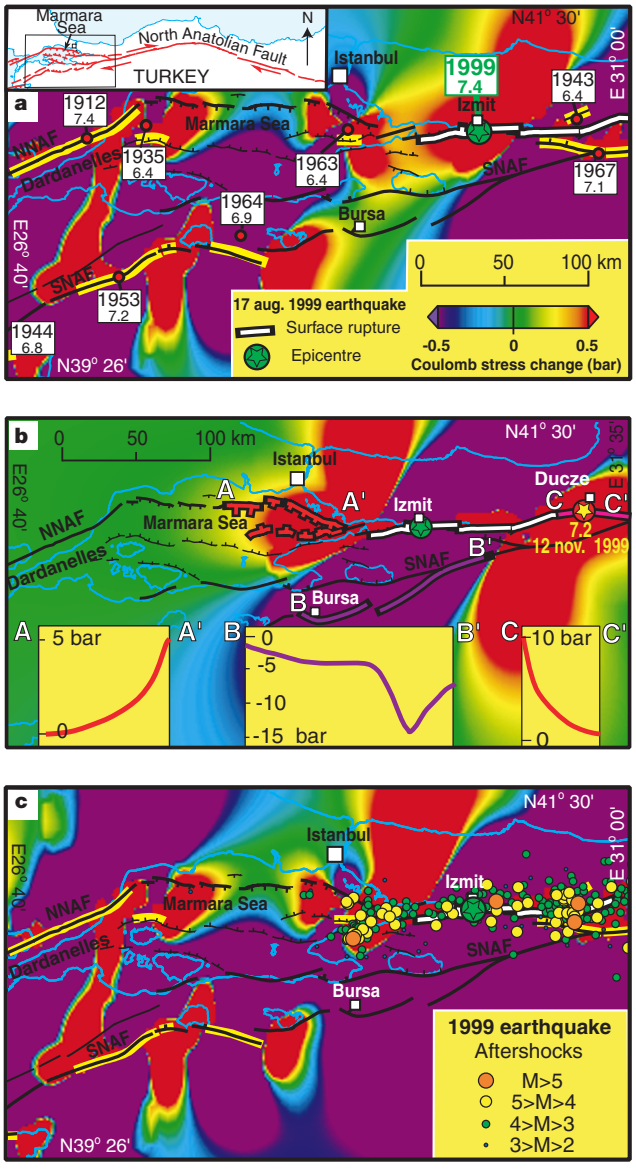

Figure 1 Stress changes due to earthquakes this century in the Marmara Sea area. These stress changes are shown at a depth of 6 km, and are calculated on optimally oriented faults (see Methods). **a,** Results for all eight $M > 6$ events before the 1999 Izmit earthquake[9]. Locations of fault elements used to model earthquakes are shown in yellow, and their epicentral location by a red dot. The area studied is shown in the inset. **b,** Stress induced by the 1999 Izmit earthquake that ruptured four on-land segments[1] (white). Rupture might have extended westward beneath the Gulf of Izmit, but is not modelled here. At the eastern tip of the Izmit rupture, fault segments (pink) between C and C' are strongly loaded by the Izmit event and ruptured during the $M = 7.2$ Ducze event on 12 November 1999. Two faults (red), west of the new rupture that bound the trough 20 km south of Istanbul are also strongly loaded. Insets show changes of Coulomb stress resolved on faults between A and A′, B and B′, and C and C′, shown respectively in red, purple and pink. The single curve in the plot A–A′ corresponds to both faults (red) as they happen to have almost identical stress loading. **c,** Stress changes due to all events since 1900. The aftershocks correlate with the stress changes, but with events notably absent in regions where the 1963 earthquake released stress.

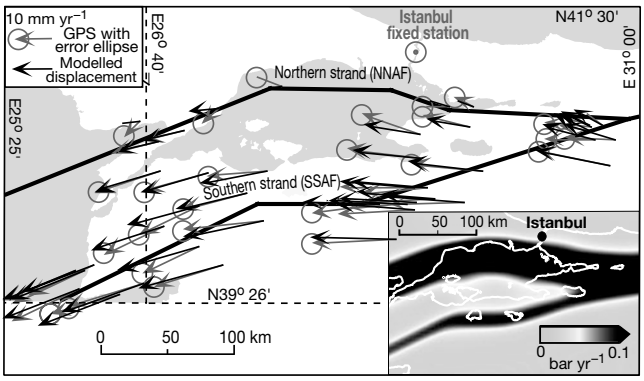

Figure 2 Model of the secular interseismic stress change. Black segments represent the location of the dislocation elements at depth, grey arrows show the observed GPS velocity field relative to the Istanbul station[11] (with circles indicating approximate daily repeatability errors[11]) and black arrows show our model fit. The inset shows the form of the stress loading at depth of 6 km. Maximum loading is 0.4 bar yr^{-1} for the NNAF, and 0.1 bar yr^{-1} for the SNAF. NNAF, northern North Anatolian fault; SNAF, southern North Anatolian fault.

sequential loading of all $M > 6$ earthquakes since 1700 (excluding the Izmit event; Fig. 3a) are taken into account to calculate the stress distribution (Fig. 3b). Models do not take into account any viscous loading[17]. The stressed region where the Izmit earthquake occurred is restricted to 40 km, and includes the epicentre and all the western segments. The segments to the east were not uniformly stressed before the earthquake (Fig. 3b), but became stressed as failure proceeded. When the effect of the Izmit event is included (Fig. 3c), regions of enhanced stress are mainly restricted to the 160-km-long Marmara Sea trough. The faults of this complex pull-apart basin have now accumulated stress over 233 years (~100 bar) without any major earthquake, and thus should be approaching failure. Much of the character of the Coulomb stress distributions is dominated by large-scale slip deficits.

To explore further these large-scale features, we examine directly the accumulating slip release due to earthquakes on the NNAF (Fig. 3d). For the period 1700–1900, the component of co-seismic slip resolved parallel to relative plate motion[3] is dominated by $M > 7$ events occurring between 1719 and 1766 (Fig. 3d). There are uncertainties in the magnitude of slip of about 1 m and the locations of segments which ruptured in each earthquake cannot be determined unambiguously, especially for the 1894 event (see discussion in Supplementary Information). This is also particularly true for the Marmara Sea pull-apart, where the fault geometry is poorly constrained: earthquakes could have ruptured north-dipping, south-dipping oblique faults or even pure strike-slip faults[12] that have a slightly different strike. However, all active faults are located in a zone 20–25 km wide, and Coulomb stress distributions for the different fault geometries at a distance from the fault plane remain similar[9]. In all the likely scenarios the westward propagating 1719–1766 sequence, which followed events farther to the east that ruptured about 500 km of the NAF in 1668[18], released all the stress previously accumulated. After 1766, stress began accumulating anew in the Marmara Sea region. After 146 years, 3.5 m of loading have accumulated on the NNAF. A single event then occurred in the west in 1912. In 1939, a major westward propagating sequence of earthquakes started rupturing the NAF from eastern Turkey to the eastern part of the Marmara Sea region ($M > 7$ earthquakes in 1957 and 1967, Fig. 3d)[6,10]. When this sequence started, at least 5 m of loading had accumulated on the NAF since 1766 as a result of plate motion. The 17 August 1999 Izmit event fills part of a 5.5-m slip deficit on the NNAF (Fig. 3d). The 12 November 1999 Ducze event ($M = 7.2$) extends the 1999 Izmit rupture zone eastwards toward the NAF fault segment that ruptured in 1944. With this last event, all the active NAF segments have now ruptured from eastern Turkey to the Sea of Marmara.

There are three possible reasons why rupture did not continue towards the west. The first could be a shadow effect resulting from the 1963 earthquake (Fig. 1a), perhaps sufficient to arrest rupture. The second could be associated with the geometry of faulting. The predominantly strike-slip faults that ruptured in 1719 and 1999 do not extend far into the eastern Marmara Sea. Motion is transferred to fault segments with substantial components of normal slip that bound the trough south of Istanbul. Thus rupture may not readily propagate directly from one fault system to the other. Finally, the Coulomb model based on our understanding of segment geometry and slip history suggests that the rupture may have been arrested by a Coulomb minimum related to earlier events as well as to the 1963 event (Fig. 3b). When the Izmit event is included, a slip gap remains within the Marmara Sea over a distance of about 160 km where 5.5 m of slip has accumulated since 1766. Unlike the NNAF, the history along the SNAF since 1700 does not provide us with a period when the whole boundary has ruptured. However, major events have occurred also in sequence west of Bursa, and none have

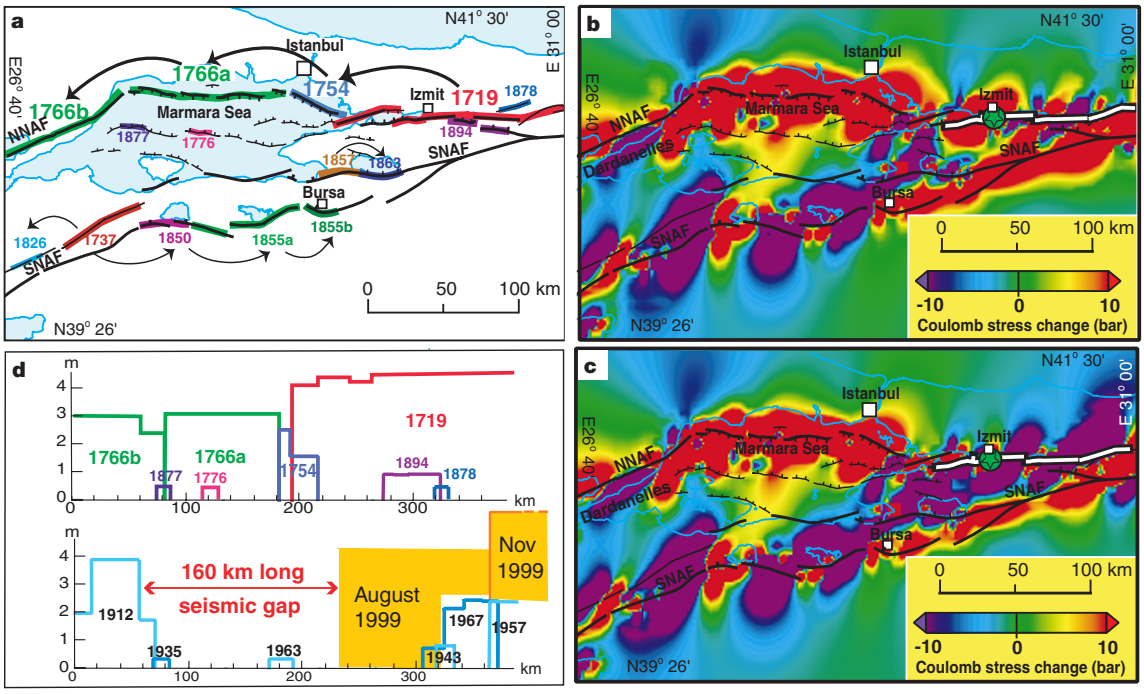

Figure 3 Earthquake-induced stress changes including historical seismicity since 1700. **a,** Location of fault elements used to model earthquakes between 1700 and 1900. **b,** Coulomb stress with tectonic loading distribution immediately before the Izmit earthquake. The 1999 earthquake epicentre is located in a high-stress area. **c,** Coulomb stress distribution with tectonic loading including the Izmit earthquake. The stresses are enhanced in the Marmara Sea area and reduced along the SNAF. **d,** Seismic slip resolved parallel to relative plate motion[3] for events on the NNAF and NAF since 1700 between longitude 26° 40′ E and 31°10′ E. In the eighteenth century, the whole Marmara region slipped (top diagram) and by 1766 most of the accumulated slip would have been released. The smaller events contribute little to the total slip. Since 1900, major events have released slip in the east and west of the Marmara Sea region (bottom diagram). The slip due to the Izmit and Ducze events fills a gap to the east.

occurred to the east in this time period. The resulting stress accumulation can be seen in the Coulomb stress distributions (Fig. 3c). The last event to have ruptured the eastern part of the fault occurred in 1419 (ref. 7). Since then, 3.5 m of slip has accumulated over 125 km of the SNAF.

The above models depend on the accuracy of our data and on assumptions about the behaviour of faults in the Marmara Sea region. It might be supposed that our slip rate of 3 cm yr^{-1} is too high. However, the earthquake slip that has occurred in the Dardanelles region (3–4 m) and in the west of the Gulf of Izmit (4–5 m) is difficult to explain if the loading rate is less. It is possible that we have over-estimated both the slip in these historical earthquakes and the loading slip. A slip rate of 2 cm yr^{-1} on the NAF would reduce all slips and slip rates by one-third, but would preserve the spatial pattern of estimated historical slip (Fig. 3d). Similar proportional changes apply to stress amplitudes in the Coulomb models. Thus changing the assumed loading rate does not alter our models. The only way to significantly change the picture would be to assume high creep rates for faults beneath the Marmara Sea. The fact that these faults have hosted numerous earthquakes throughout history makes this improbable.

The significance of the observations here can be clarified by discussing the slip deficits and Coulomb stress changes together. A major slip gap (5.5 m since 1766) exists on faults beneath the Marmara Sea, and might be greater than the slip released by events in 1754 and 1766 following the 1719 earthquake (Fig. 3d). Faults in the west and east of the Marmara Sea region have experienced Coulomb stress increases due to events this century (Fig. 1). The stress increase in the west has been present since the 1912 earthquake while that in the east has just happened. In 1719 when an event similar to the Izmit event occurred, it was followed 35 years later (in 1754) by an event on a fault to the west. The same fault has now experienced a Coulomb stress increase of 1–5 bar (Fig. 1b). It is therefore likely that this fault will slip again and furthermore, the risk during the aftershock sequence must be regarded as particularly high[10,19]. Following the 1754 earthquake, the 1766 events ruptured the rest of the fault 12 years later. It is very likely that a similar sequence will recur.

From the present study, the NAF earthquake behaviour could be summarized in the following way. Stress accumulates on the fault continuously as a result of plate motion. When the whole fault system is near failure, a critical stage is reached that is characterized by an extreme susceptibility to small perturbations and strong correlation between different parts of the system[20,21]. Small stress increases (1–5 bar) are then sufficient to trigger failure in the upper crust, and the fault tends to rupture over most of its length in a cascading sequence of earthquakes. Between 1668 and 1766, the NAF seems to have ruptured over most of its length in such a sequence in about 100 years. This century the fault ruptured from eastern Turkey to the Izmit bay in a sequence of eight $M > 7$ events, the Izmit and the Ducze earthquakes being the last ones. In the next decades, it is likely that rupture of the fault segments of the Marmara Sea region will complete the sequence. □

Methods

Coulomb modelling

The stress fields due to earthquakes are calculated using dislocation theory[8,22]. Dislocations to represent each event or sub-event are approximated by rectangular planes whose geometry, dimension and location must be known. Places of likely future failure are then identified as having an increased Coulomb stress ($\Delta\sigma_f$), which is calculated at a depth of 6 km (ref. 9; $\Delta\sigma_f = \Delta\tau - \mu' \Delta\sigma_n$ with $\mu' = 0.4$, where $\Delta\tau$ and $\Delta\sigma_n$ are respectively the change in shear and normal stresses on likely future fault planes). To specify preferred orientations of faulting, a regional stress is applied and the program searches for the optimal strike, dip and rake of the fault unless it is specified (horizontal principal compressive stress axis of 100–150 bar oriented N120°E)[8,9]. All fault dislocations extend from the surface to a depth of 15 km, which is slightly greater than the 12.5 km previously used[9] to be consistent with the loading model. In the program, $\Delta\tau = \Delta e_{13} + \Delta e_{31}$ (where $\Delta\tau$ is the shear stress on the target fault plane, and Δe_{13} is the tensor component of shear stress rotated into that plane), so the calculated Coulomb stresses are to a first approximation doubled when compared to previous work[8,9,10] where $\Delta\tau = \Delta e_{13}$.

Tectonic loading

This is modelled by dislocations assumed to extend through the lithosphere to infinite depth (this is similar to a dislocation extending to 100 km and a fluid asthenosphere beneath). The slip parameters for these deep dislocations were established to fit the following criteria. The overall rate should be consistent with recent geological rates (2.0 cm yr^{-1})[4,5], geodetic rates (2.5–3.0 cm yr^{-1})[3], a reasonable Europe/Anatolia pole of rotation[3,4] and the locally measured GPS rates around the Marmara Sea[11]. To fit this data, a 3.0 cm yr^{-1} slip (0.6 cm yr^{-1} on the SNAF, 2.4 cm yr^{-1} on the NNAF) is needed. We reduced slightly the component of opening on the NNAF consistent with the pole to fit local GPS vectors. The depth used was 15 km. In fact, reasonable fits with local GPS could be obtained with locking depths of 10–20 km (ref. 23). However, a locking depth of 10 km seems too small to generate an earthquake of $M = 7.4$, while a locking depth of 20 km requires the slip to be increased to nearly 3.5 cm yr^{-1}, which seems too high.

Fault parameters for earthquakes from 1700 to 1900

All of the $M > 6$ earthquakes in Turkey produce surface faulting that accumulates to produce recognisable morphological features. These allow fault geometry to be mapped, each fault segment having characteristic parameters (length, strike, dip and rake). When this information is combined with historical data describing damage, seismic sea-waves or liquefaction, all of the parameters of earlier earthquakes can be evaluated[9]. Historical records of fifteen $M > 6$ earthquakes exist in the area around Istanbul for 1700 to 1900 (ref. 7). The catalogue separates events into those with $M > 7$ and those with $6 \leq M < 7$, with $M > 7$ events breaking 2 or more segments while the smaller ones occur on single segments. Segments associated with an event are initially identified mainly from reported damage. Scaling relations[15] are used to determine magnitude and moment. Slip is then distributed between the dislocations representing the segments. The slip direction is taken to be parallel to the relative plate motion[3]. The final parameters are adjusted using two additional criteria. First, if one event was clearly larger than another, its magnitude should be greater and it should involve a greater length of faulting. Second, unless there is clear evidence that two events occupied the same stretch of fault, they are more likely to have occurred on adjacent segments. An example of the former is provided by the 1719 and 1999 events. Damage in the 1719 and 1999 events occurred in the same places. However, in 1719 there was widespread damage in Istanbul. If such shaking had been repeated in 1999 much greater destruction would have occurred in Istanbul. We therefore conclude that, in addition to the segments that ruptured in August and November 1999, a sub-marine segment closer to Istanbul also ruptured in 1719. An example of the latter is provided by events in 1719, 1754, 1766a and 1766b, which occurred in a westward migrating sequence. These events are placed such that every segment of this stretch of fault moved once. Defining the slip regions for the six largest events is more straightforward than estimating parameters of some smaller events, for which there can be a choice of two or even three possible locations separated by 20 km or more. For example the 1894 event had a damage area similar to the 1999 and 1719 events, but the associated destruction was much less, so its rupture zone should be shorter and reduced to one or two fault segments (see Supplementary Information). However, as these events contribute little to the overall slip, errors in their location have no significant effect on the conclusions we report here.

Received 6 September 1999; accepted 31 January 2000.

1. Barka, A. A. 17 August 1999 Izmit earthquake. *Science* **258,** 1858–1859 (1999).
2. Barka, A. A. The North Anatolian Fault zone. *Ann. Tectonicae* **VI** (suppl.), 164–195 (1992).
3. Reilinger, R. E. *et al.* Global Positioning System measurements of the present-day crustal movements in the Arabia-Africa-Eurasia plate collision zone. *J. Geophys. Res.* **102,** 9983–9999 (1997).
4. Hubert, A. *La Faille Nord-Anatolienne (Cinématique, Morphologie, Localisation, Vitesse et Décalage Total) et Modélisations Utilisant la Contrainte de Coulomb sur Différentes Echelles de Temps.* Thesis, Denis Diderot Univ., Paris VII (1998).
5. Armijo, R., Meyer, B., Hubert, A. & Barka, A. Westward propagation of the North Anatolian fault into the northern Aegean: Timing and kinematics. *Geology* **27,** 267–270 (1999).
6. Ambraseys, N. N. Some characteristic features of the North Anatolian fault zone. *Tectonophysics* **9,** 143–165 (1970).
7. Ambraseys, N. N. & Finkel, C. Long-term seismicity of Istanbul and of the Marmara Sea region. *Terra Nova* **3,** 527–539 (1991).
8. King, G. C. P., Stein, R. S. & Lin, J. Static stress changes and the triggering of earthquake. *Bull. Seismol. Soc. Am.* **84,** 935–953 (1994).
9. Nalbant, S. S., Hubert, A. & King, G. C. P. Stress coupling between earthquakes in northwest Turkey and the north Aegean Sea. *J. Geophys. Res.* **103,** 24469–24466 (1998).
10. Stein, R. S., Barka, A. A. & Dieterich, J. H. Progressive failure on the North Anatolian fault since 1939 by earthquake stress triggering. *Geophys. J. Int.* **128,** 594–604 (1997).
11. Straub, C., Khale, H. G. & Schindler, C. GPS and geological estimates of the tectonic activity in the Marmara Sea region, NW Anatolia. *J. Geophys. Res.* **102,** 27587–27601 (1997).
12. Barka, A. A. & Kadinsky-Cade, K. Strike-slip fault geometry in Turkey and its influence on earthquake activity. *Tectonophysics* **7,** 663–684 (1988).
13. Harris, R. A. Stress triggers, stress shadows and implications for seismic hazard. *J. Geophys. Res.* **103,** 24347–24358 (1998).
14. Harris, R. A. & Simpson, R. W. In the shadow of 1857- Effect of the great Ft. Tejon earthquake on subsequent earthquakes in southern California. *Geophys. Res. Lett.* **23,** 229–232 (1996).
15. Kanamori, H. & Anderson, D. L. Theoretical basis of some empirical relations in seismology. *Bull. Seismol. Soc. Am.* **65,** 1073–1095 (1975).
16. Wittlinger, G. *et al.* Tomographic evidence for localized lithospheric shear along the Altyn Tagh fault. *Science* **282,** 74–76 (1998).

17. Pollitz, F. F. & Dixon, T. H. GPS measurements across the northern Caribbean plate boundary zone; impact of postseismic relaxation following historic earthquakes. *Geophys. Res. Lett.* **25,** 2233–2236 (1998).
18. Ambraseys, N. N. & Finkel, C. F.in *Historical Seismograms and Earthquakes of the World* (eds Lee, W. H. K., Meyers, H. & Shimazaki, K.), 173–180 (Academic, San Diego, 1988).
19. Dieterich, J. A constitutive law for rate of earthquake production and its application to earthquake clustering. *J. Geophys. Res.* **99,** 2601–2618 (1994).
20. Sornette, A. & Sornette, D. Self organized criticality and earthquake. *Europhys. Lett.* **9,** 197 (1989).
21. Bowman, D. D. *et al.* An observational test of the critical earthquake concept. *J. Geophys. Res.* **103,** 24359–24372 (1998).
22. Okada, Y. Internal deformation due to shear and tensile fault in a half-space. *Bull. Seismol. Soc. Am.* **82,** 1018–1040 (1982).
23. Segall, P. & Harris, R. Slip deficit on the San Andreas Fault at Parkfield, California, as revealed by inversion of geodetic data. *Science* **233,** 1409–1413 (1986).

Supplementary information is available on *Nature*'s World-Wide Web site (http://www.nature.com) or as paper copy from the London editorial office of *Nature*.

Acknowledgements

We thank F. F. Pollitz and R. Harris for comments on the manuscript. This work was supported by the EEC FAUST programme and the INSU-CNRS PNRN programmes.

Correspondence and requests for materials should be addressed to A.H.-F. (e-mail: ferrari@princeton.edu).

Fine-scale heterogeneity in the Earth's inner core

John E. Vidale*† **& Paul S. Earle***

Earth and Space Science Department and Institute of Geophysics and Planetary Physics†, University of California at Los Angeles, Los Angeles, California 90095-1567, USA*

The seismological properties of the Earth's inner core have become of particular interest as we understand more about its composition and thermal state[1,2]. Observations of anisotropy and velocity heterogeneity in the inner core are beginning to reveal how it has grown and whether it convects[3,4]. The attenuation of seismic waves in the inner core is strong, and studies of seismic body waves[5,6] have found that this high attenuation is consistent with either scattering or intrinsic attenuation[5]. The outermost portion of the inner core has been inferred to possess layering and to be less anisotropic than at greater depths[7–10]. Here we present observations of seismic waves scattered in the inner core which follow the expected arrival time of the body-wave reflection from the inner-core boundary. The amplitude of these scattered waves can be explained by stiffness variations of 1.2% with a scale length of 2 kilometres across the outermost 300 km of the inner core. These variations might be caused by variations in composition, by pods of partial melt in a mostly solid matrix or by variations in the orientation or strength of seismic anisotropy.

Here we examine 12 earthquakes and 4 nuclear explosions in the distance range 58° to 73°. The events, listed in Table 1, were recorded on LASA (Large Aperture Seismic Array) between 1969 and 1975, and were less than 100 km deep. LASA consisted of up to 525 short-period vertical-component seismometers buried to a depth of 70 m and spread across an aperture of 200 km in Montana[11,12].

Our seismograms mostly extend from the P wave back past the P′P′ arrival, spanning more than half an hour. An arrival that is not explained by previously identified ray-paths appears near the predicted arrival time for PKiKP, which is the faint reflection from the boundary between the inner and outer core. Generally, the boundary between the inner and outer core appears locally flat and sharp[8,13,14]. Figure 1 shows the onset time, duration, and slowness of the energy incident on LASA in this interval. The image is the logarithmic average of slant stacks of the 16 events generated from the seismograms after they had been passed through a 1-Hz band-pass filter.

We attribute the 200 s of observed ground motion to inner-core scattering (ICS) (Fig. 1). This energy arrives nearly vertically from the direction of the inner core. The energy builds for a few tens of seconds, then gradually fades back into the more omnidirectional background. Most of the energy lies between –0.02 and 0.02 s km^{-1}, consistent with paths from the inner core. The initial tens of seconds of the ICS have an average slowness near 0.01 s km^{-1}, close to that expected for PKiKP. These unexpected arrivals are not visible in the seismograms without stacking. PKiKP is barely visible, as expected at these distances[8,14,15].

Also visible in Fig. 1 is a comparable amount of energy with the same slowness as the direct P wave, which also fades with time. This late-arriving P coda is scattered near the event. LASA is sufficiently dense and wide to clearly distinguish between the inner-core arrivals and the P coda. The background noise is generated by the event; it diminishes monotonically with increasing time after the event, and is higher than the pre-event noise.

Our 16 events sample four distinct regions of the inner core (Fig. 2a). The ray paths of PKiKP and the ICS are shown in Fig. 2b. Many of the earthquakes occurred near Japan, and the explosions were in Novaya Zemlya; there were also earthquakes under Peru and

Table 1 Earthquakes and explosions in this study

Date dd/mm/yr	Time	Latitude (°N)	Longitude (°E)	Depth (km)	Distance
28/02/69	04:25:36.9	36.23	–10.48	33	68°
31/05/70	20:23:27.3	–9.18	–78.82	33	68°
02/08/71	07:24:56.0	41.37	143.44	45	73°
05/09/71	18:35:26.8	46.54	141.15	14	70°
06/09/71	13:37:10.1	46.76	141.39	21	70°
09/09/71	23:02:06.8	44.34	150.85	7	69°
27/09/71	05:59:55.8	73.39	54.92	0	59°
24/11/71	19:35:28.5	52.85	159.22	99	57°
28/02/73	06:37:54.4	50.51	156.58	62	60°
17/06/73	20:37:52.1	42.65	146.08	11	70°
24/06/73	02:43:22.8	43.29	146.43	26	70°
27/10/73	06:59:58:0	70.80	53.96	0	62°
15/05/74	18:59:56.1	49.98	156.22	58	60°
29/08/74	09:59:56.2	73.39	54.91	0	59°
09/10/74	07:32:00.6	44.64	150.09	34	67°
02/11/74	04:59:57.4	70.83	53.82	0	62°

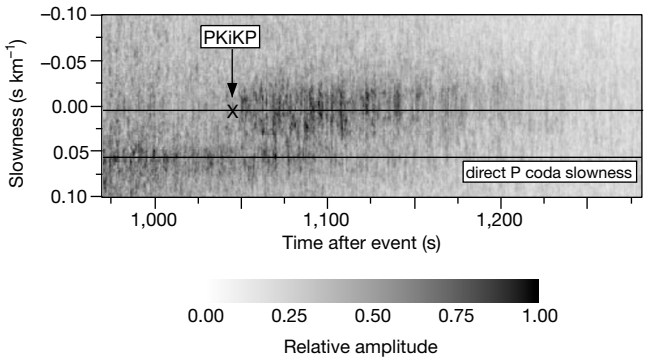

Figure 1 Average seismic-wave amplitude arriving between 970 and 1,280 s after all events. The image shows logarithmically averaged envelopes of the slant stacks for all 12 earthquakes and 4 nuclear explosions. The image shows the time and slowness, which is the reciporcal of apparent velocity, of energy incident on LASA. Three features of the signal are visible: (1) a stripe near 0.06 s km^{-1} slowness, which corresponds to late P coda and aftershocks, (2) a stripe of energy from 1,050 s until 1,250 s that we interpret as inner-core scattering (ICS), and (3) uniform background source-generated noise that diminishes with time. All subarrays are included in this stack for maximum slowness resolution.